Fault Tolerance Converter with Modular Structure for HVDC Power Transmitting Applications

Yihua Hu, *Senior Member, IEEE*, Guipeng Chen, *Student Member, IEEE*, Yang Liu, *Student Member, IEEE*, Lin Jiang, *Member, IEEE*, Peng Li, *Member, IEEE*,

***Abstract*—For the high-voltage direct-current (HVDC) power transmission system of offshore wind power, DC/DC converters are the potential solution to collect the power generated by off-shore wind farms to HVDC terminals. The converters operate with high voltage gain, high efficiency, and fault tolerance over a wide range of operating conditions. In this paper, an isolated ultra-high step-up DC/DC converter with a scalable modular structure is proposed for HVDC offshore wind power collection. A flyback-forward converter is employed as the power cell to form the expandable electrically-isolated modular DC/DC converter. The duty ratio and phase shift angle control are also developed for the proposed converter. Fault tolerance characteristics of the converter are illustrated through the redundancy operation and fault ride-through tests. Redundancy operation is designed to maintain high operation efficiency of the converters and fault ride-through operation improves the converter reliability under harsh operating conditions. Analytical studies are carried out, and a 750 W prototype with three modular cells is built and experimentally tested to verify the performance of the proposed modular DC/DC converter.**

***Index Terms*—DC/DC converters, high step-up, HVDC, scalability, wind power generation.**

I. Introduction

Wind power generated by offshore wind farms needs to be transferred to the onshore grid through long distance transmission lines. The transmission system should be economic, efficient, reliable, and environmentally friendly [1]-[7]. Recently, extensive studies are undertaken on the high-voltage direct-current (HVDC) subsea transmission for the long-distance large-scale offshore wind farms, which leads to lower cable losses and higher efficiency in comparison to the conventional HVAC transmission systems [8]-[15].

In the existing literature, two kinds of configurations are usually employed to ensure the system feasibility [12][13]. The first one is as shown in Fig. 1 (a), in which the offshore wind turbines is connected to a micro AC grid. The voltage step-up is realized by a line frequency high ratio transformer. Resonances occur frequently in the AC micro grid in the cases where the receiving-end AC grid is weak. The other one is as shown in Fig. 1 (b) and Fig. 1 (c), in which the wind turbines are connected to the HVDC transmission system through DC/DC converters. This kind of configuration can effectively avoid grid resonance. Different from the AC connection, the DC connection faces the difficulty of voltage step-up. The DC connection includes topologies. The first topology is as shown in Fig. 1 (b), which includes two step-up DC/DC conversion stages between the low voltage turbine generators and the HVDC terminals. The system demonstrates advantages in aspects of enhanced fault ride-through capability and easy converter design. The two DC/DC conversion stages are required to step up a low voltage (LV) to a medium voltage (MV), and then to a high voltage (HV) [16]. Although the wind turbine generator can be developed to increase its output voltage (up to 4 kV), the step up ratio at each DC/DC conversion stage is expected to be at least 1:10 to meet the HVDC transmission requirements [15].

From a theoretical point of view, the two stage DC/DC conversion can be simplified as a one-stage DC/DC conversion, as shown in Fig. 1 (c). The DC/DC converter can step up the voltage directly from the LV to HV without a MV grid. In this case, the converter design is a technical challenge since the ultra-high voltage gain, such as 1:100, becomes mandatory. Luckily, the fast developments of semiconductors and converter topologies make the solution feasible [17]-[22]. When the transformers are utilized to achieve high voltage gain in DC/DC converters, the high conversion gain can be achieved by manipulating the winding turn ratio. However, a very high turn ratio should always be avoided in the transformer design since it reduces the energy conversion efficiency [23]. Therefore, for the single stage DC/DC conversion, the DC/DC converter should achieve both high voltage gain and high conversion efficiency over a wide power range.

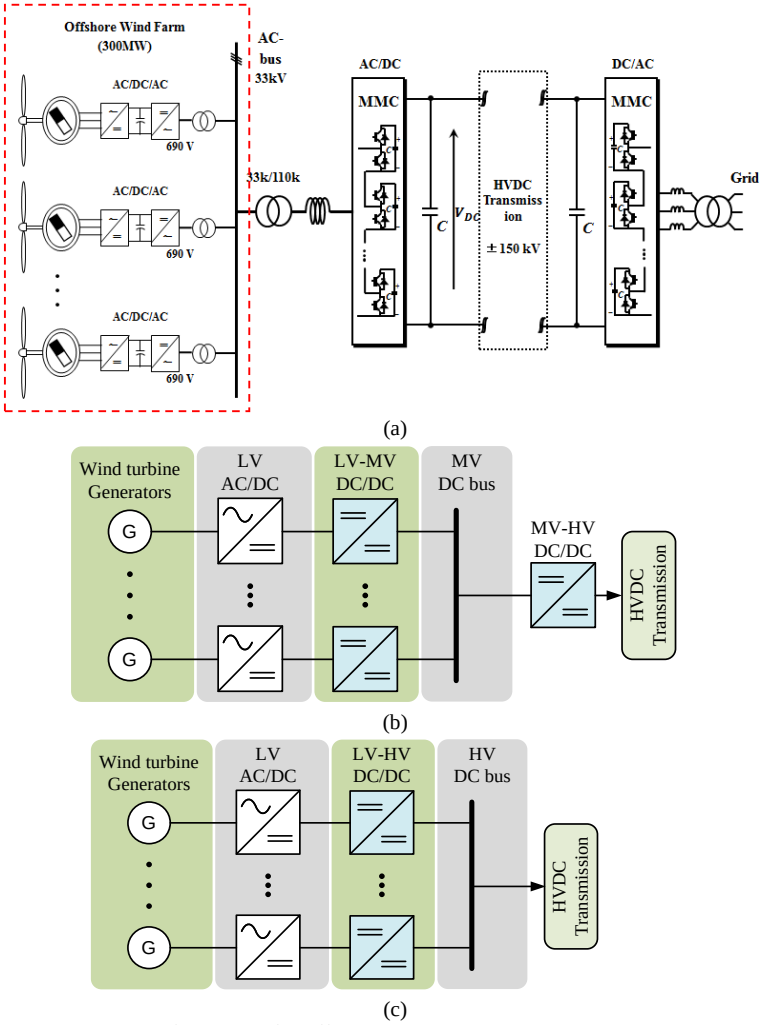

Fig. 1. HVDC configurations for offshore wind power transmission. (a) AC based connection for HVDC (b) DC based connection with two-stage DC/DC conversion and (c) DC based connection with one-stage DC/DC conversion.

A resonant switched-capacitor topology was presented in [24] for offshore wind farms to connect various kinds of HVDC systems,

which demonstrated the advantages of soft switching to minimize the switching losses. However, its achievable conversion ratio is only 1:7, which is not suitable for the single stage configuration. A multiphase resonant DC/DC topology was thus developed in [25] to step up the voltage level from LV to MV. In [26], a conventional non-isolated DC/DC converter was used as the building block to build up the conversion gain. The technique of building HVDC links with modular multilevel converters was proposed in [21]. With a resonant technique, the multilevel converter can also be developed as a step-up DC/DC converter [27]. [28] and [29] proposed the topology of series connection of the output terminal to achieve a high voltage gain, but the proposed topology does not provide electrical isolation or modular structure. Paper [30] investigated a dual-active bridge converter for high-voltage high-power applications. Nonetheless, it uses a complex control strategy to achieve current sharing among power cells. Based on the forward-flyback converter and interleaved working method, paper [31] described a multi-phase DC/DC converter to achieve a high voltage gain, but it does not provide electrical isolation. Paper [32] employed thyristors as the switching devices and developed a LCL DC/DC converter for offshore HVDC applications. But the voltage step-up ratio is relatively low. Paper [33] developed a multilevel converter based on the push–pull converter. Although the input and output can share a common ground, it does not provide electrical isolation. A high power level DC/DC converter was realized in [34] with an alternate arm converter (AAC) and a modular multilevel converter (MMC) topology, while the high frequency high power level transformer is the bottleneck of the system. Paper [35] developed a series–parallel topology with multi outputs. The secondary side series structure was also employed in [36] to achieve high voltage gain. However, the complex structure limits its extendibility. Paper [37] presented a good solution for high voltage gain and high power level converters, which is more suitable for wind farm connection with HVDC system, as shown in Fig. 1 (b). Currently, none of the existing studies have figured out a converter with modular structure and fault tolerance capability, which can achieve the LV-HV conversion in HVDC applications. Because the following criteria should be satisfied:

(i) Hardware

Modular structure; electrical isolation; high voltage gain; each power converter cell should be decentralized to avoid power stress concentration.

(ii) Software

Due to the requirement of ultra-high voltage gain, flexible control of the converter should be explored.

(iii) Fault tolerance

The converter should be able to work in the cases where internal or external faults occur.

In order to achieve those requirements, this paper proposes a novel ultra–high step-up DC/DC converter using advanced control strategies and applying current sharing techniques to power cells in the converter. In this paper, Section II introduces the proposed converter topology; Section III develops the corresponding control strategy. In Section IV, an experimental rig is built to verify the proposed converter topology and control strategy, followed by Section V to conclude the paper.

II. Proposed Scalable Topology

A. Basic cell structure

Fig. 2 (a) shows the basic cell structure of the proposed converter. Its primary side consists of four switches, two coupled inductors, and a clamped capacitor, and its secondary side consists of two coupled inductors serially connected with reverse polarity. Fig. 2(b) shows the scalable structure of the proposed topology. On the primary side, all the cells are parallel connected. On the secondary side, the cells are connected by a diode bridge. The cells can be organized and scaled according to the power level and output voltage level requirements. With the development of SiC MOSFET devices, 10 kV voltage level is achievable [38]. Therefore, MOSFETs are employed as switching devices for the DC/DC converter proposed in this paper.

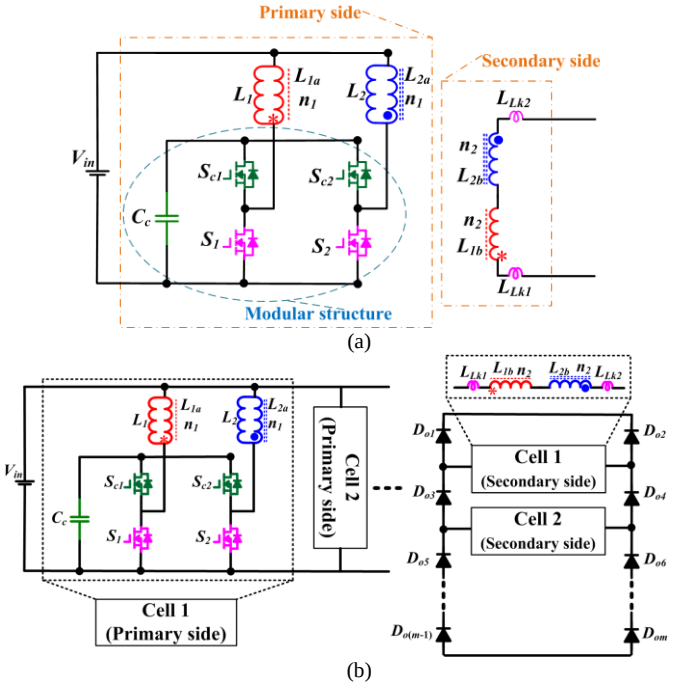

Fig. 2. The proposed modular DC/DC converter. (a) Basic cell structure and (b) Expandability of the topology.

B. Operation of the two-cell topology

Based on the proposed general topology, a two-cell topology is deduced, which is shown in Fig. 3. S_1~S_4 are the main switching devices; S_{c1}~S_{c4} are the active clamping switching devices; C_c is the clamping capacitor; L_1~L_4 are the coupled inductors, and the corresponding coupling references are remarked with "*", "○", "□" and "▌". The turns number of the primary and secondary windings of the coupled inductors are represented by n_1 and n_2, respectively, and their turns ratio is $N = n_2/n_1$. The leakage inductances are termed as L_{LK1}-L_{LK4} for the coupled inductors L_1-L_4, respectively. The secondary-side rectifier diodes are termed as D_{o1}-D_{o6}. L_1, L_2 and the corresponding switching devices form cell-1; L_3, L_4 and the corresponding switching devices form cell-2.

The steady-state waveforms of the two-cell converter are plotted in Fig. 4. In this figure, the main switching devices use the same duty ratio (0.5) and the active clamping switches S_{C1} - S_{C4} conduct in a coordinated manner with the corresponding main switches. In the cell, the phase shift angle between the main switching devices is 180°; and the phase shift angle between cells is also 180°. The output voltages of cell-1 and cell-2 are V_{ab} and V_{cd}, respectively.

There are four basic working states for the two-cell topology, as shown in Fig. 5.

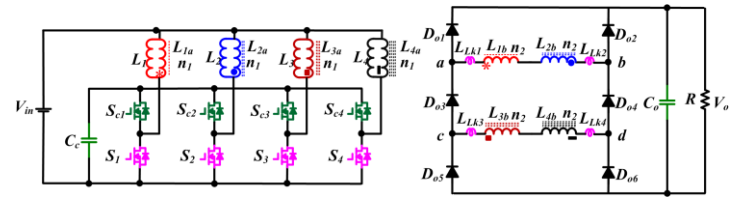

Fig. 3. The two-cell topology

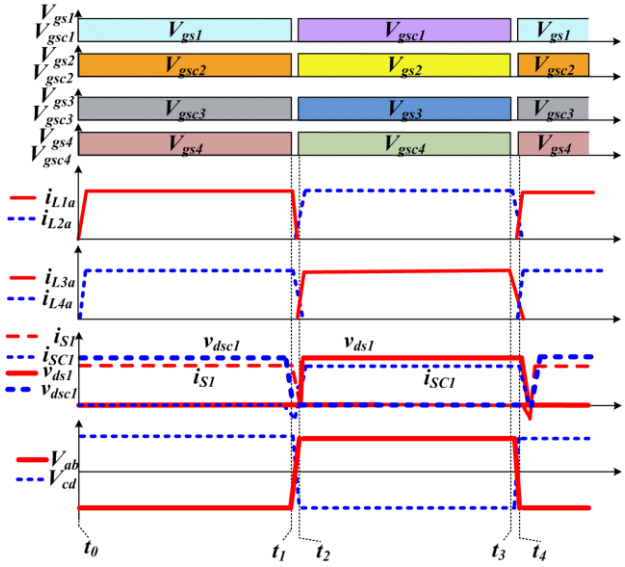

Fig. 4. Output waveforms of the two-cell topology.

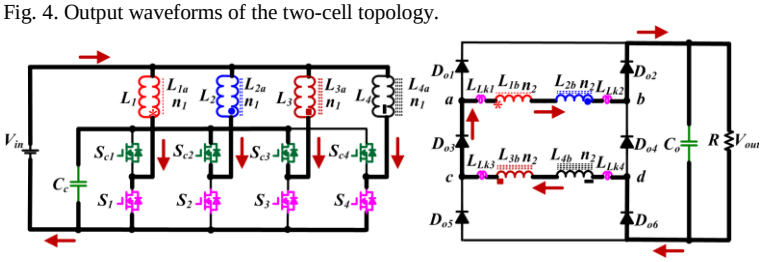

(a)

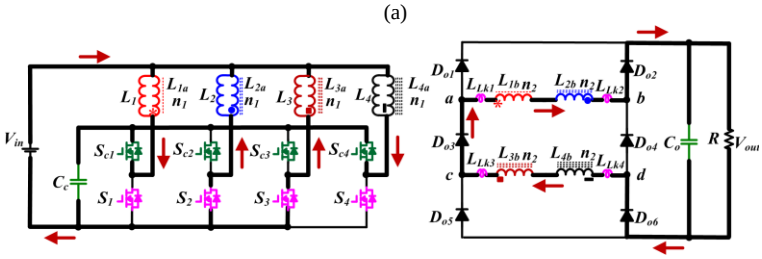

(b)

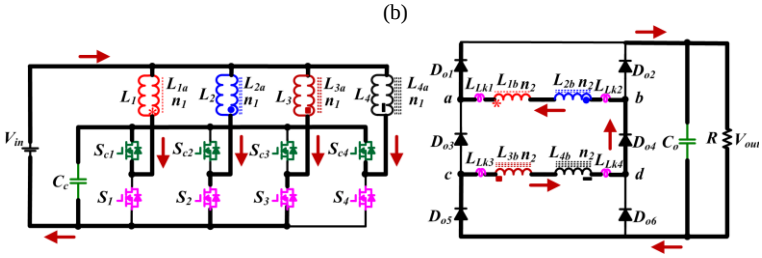

(c)

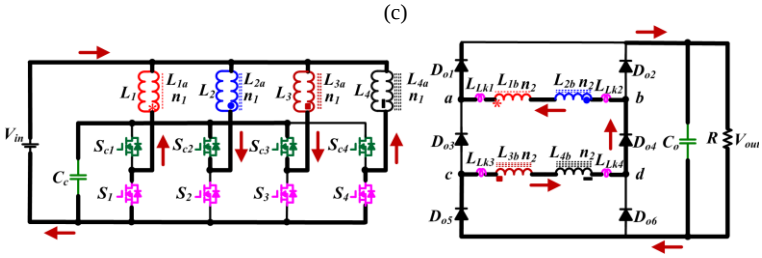

(d)

Fig. 5. Working stages of the two-cell converter. (a) Stage 1 (t_0~t_1). (b) Stage 2 (t_1~t_2). (c) Stage 3 (t_2~t_3) and (d) Stage 4 (t_3~t_4)

State 1 [t_0, t_1]: During this stage, the main switches S_1 and S_4 are turned on, while S_2 and S_3 are turned off. The clamping switches S_{c1} and Sc4 are in turn-off state; the clamping switches S_{c2} and S_{c3} are in turn-on state. For cell-1, L_1 is working in the forward mode, and L_2 is working in the flyback mode. For cell-2, the main switching devices S_4 conducts and enables L_4 to work in the flyback mode, and L_3 is working in the forward mode. In this stage, the secondary-side currents of cell-1 and cell-2 are reverse and go through D_{o2}, D_{o3} and D_{o6} to the load.

State 2 [t_1, t_2]: At t_1, the main switches S_1 and S_4 receive a turn-off gate signal, increasing their drain-source voltage stress in an approximately linear way to the parasitic capacitor of the main switches. Due to the low capacity of the parasitic capacitor and the large current on the primary-side of the coupled inductor, this period is very short. At t_1, the clamping switches S_{c2} and S_{c3} receive a turn-off gate signal, Due to the parasitic capacitor in main switches S_2 and S_3, the drain-source voltage of the switching devices S_2 and S_3 decreases linearly and the corresponding clamping switching devices (S_{c2} and S_{c3}) increase linearly. In this stage, the switching devices can achieve soft switching.

State 3 [t_2, t_3]: At t_2, the main switches S_2, S_3, S_{c1} and S_{c4} receive a turn-on signal, respectively. For cell-1, L_2 is working in the forward mode while L_1 is working in the flyback mode. For cell-2, L_3 works in the flyback mode and L_4 works in the forward mode. During this stage, the secondary-side currents of cell-1 and cell-2 are reverse, which go through D_{o1}, D_{o4}, and D_{o5} to the load.

State 4 [t_3, t_4]: At t_3, the main switches S_2 and S_3 receive a turn-off gate signal, respectively. The drain-source voltage stress on the parasitic capacitor of the main switches increases. This period is very short. At t_3, the clamping switches S_{c1} and S_{c4} receive the turn-off gate signal, the drain-source voltage of the switching devices S_1 and S_4 decreases linearly and the corresponding clamping switching devices (S_{c1} and S_{c4}) increase linearly. In this stage, the switching devices can achieve soft switching.

C. *Operation of the topology with more than two cells*

When the number of cells is more than two, odd-number of cells and even-number of cells can form two different types of the proposed topology. Fig. 6 presents the former topology. There are two current flow states on the secondary-side as illustrated in Fig. 7. In Fig. 7, cell 1 and cell 2 have a reverse polarity and so do cell 2 and cell 3. Cell 1 and cell 3 have the same polarity in two current flow states. In current flow state 1, the current passes through D_{o2}, D_{o3}, D_{o6}, and D_{o7}. In current flow state 2, the current goes through D_{o1}, D_{o4}, D_{o5}, and D_{o8}. Fig. 8 presents the latter topology; there are also two current flow states on the secondary-side. As illustrated in Fig. 9, cell 1 and cell 3 have the same polarity and so do cell 2 and cell 4. Cell 1 and cell 2 have a reverse polarity. In current flow state 1, current passes through D_{o1}, D_{o4}, D_{o5}, D_{o8}, and D_{o9}. In current flow state 2, the current flows through D_{o2}, D_{o3}, D_{o6}, D_{o7}, and D_{o10}.

From the analysis of the converter with odd number of cells (3 cells) and the converter with even number of cells (4 cells), a high voltage gain can be achieved by connecting the secondary terminals of all cells in series. Therefore, the adjacent cells on the secondary-side should have a reverse polarity, which is realized by adding 180° phase shift between adjacent cells primary switching devices.

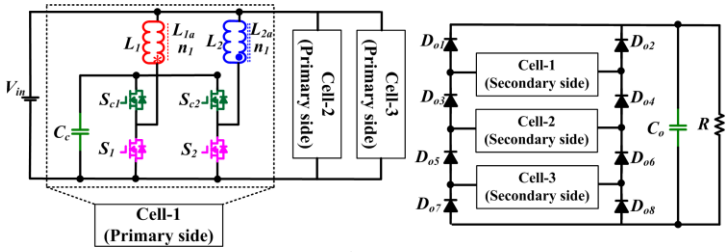

Fig. 6. The topology with odd number of cells.

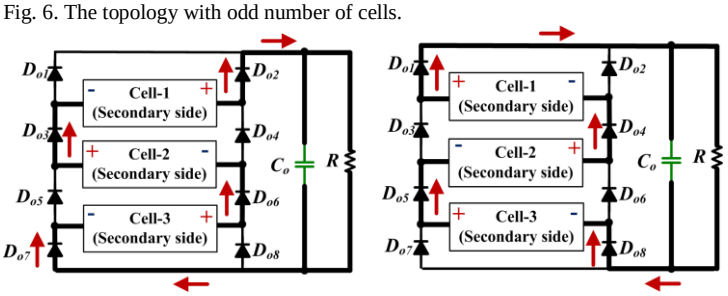

(a) (b)

Fig. 7. Two secondary current states for the topology with odd number of cells. (a) State 1 and (b) State 2.

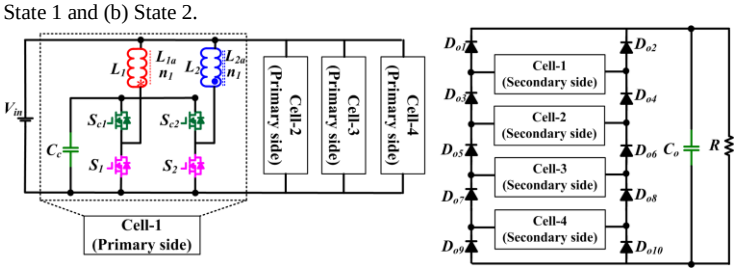

Fig. 8. The topology with even number of cells.

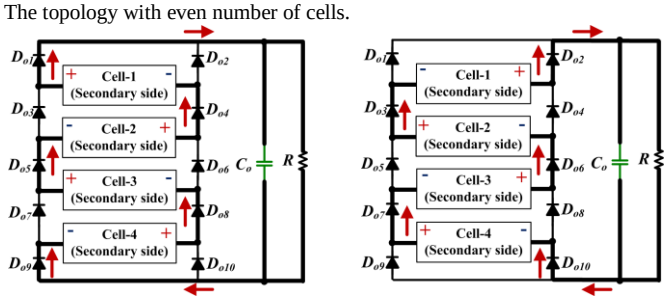

(a) (b)

Fig. 9. Two secondary current states for the topology with even number of cells. (a) State 1 and (b) State 2.

D. Steady-state performance

In order to obtain a concise mathematic expression of the proposed topology, the following assumptions are made,

i) The leakage inductance is ignored.

ii) The voltage drop on the solid state devices is ignored.

iii) The parasitic resistance of capacitors and coupled inductors are ignored.

On the primary-side, the voltage stress on the main switches and clamp switches can be expressed as

$$V_{ds} = \frac{V_{in}}{1-D} \tag{1}$$

where D is the duty ratio of main switches, V_{in} is the converter input voltage.

The voltage on the clamp capacitor can be expressed as

$$V_{Cc} = \frac{V_{in}}{1-D} \tag{2}$$

From (1) and (2), the voltage stress on primary-side switching devices and capacitor are low.

On the secondary-side, there are two types of diodes used. One type is the terminal rectification diodes (e.g. D_{o1}, D_{o2}, D_{o9}, and D_{o10} presented in Fig. 9) and the other type is the middle rectification diodes (e.g. D_{o3}~D_{o8} shown in Fig. 9). Since the terminal rectification diode is only linked with one cell, the corresponding voltage stress can be expressed as

$$V_{D1} = \frac{N}{1-D} \tag{3}$$

where N stands for turns ratio (n_2/n_1) of coupled inductor.

Because the middle rectification diode is linked with two cells, the corresponding voltage stress can be expressed as

$$V_{D2} = \frac{2N}{1-D} \tag{4}$$

If the adjacent cells have a 180° phase shift and the coupled inductors share the same turn ratio, the output voltage is the sum of the voltage of all cells connected in series of the rectifier. The voltage gain can then be expressed as

$$G = \frac{V_{out}}{V_{in}} = \frac{mN}{1-D} \tag{5}$$

where m is the cells number, V_{out} is the converter output voltage.

III. Control Strategy for the Proposed Topology

For the flexible control of the proposed converter, duty ratio control, phase shift control, redundancy control, and fault-tolerant control methods are designed. In traditional low voltage DC/DC converters, both duty ratio and phase shift control can be employed to control the output voltage precisely. While in high voltage gain DC/DC converter, when the number of working cells is large, the duty ratio cannot be employed as the control variable alone. According to (5), a small change of duty ratio can result in a significant variation of the voltage output. Therefore, duty ratio or phase shift angle cannot be employed as the control variable alone. The proposed topology has modular structure, and the modular cells can be switched on or switched off conveniently. Therefore, the number of working cells can also be employed as a control variable to achieve precise voltage control. Under low voltage deviation conditions, the control of working cell number can offer more smooth voltage change, which ensures more precise control of the voltage output. Under high voltage deviation conditions, the duty ratio or phase shift angle control can be employed as control variables to track the voltage reference rapidly.

The above four control schemes are explained in detail in the following.

A. Duty ratio control

The duty ratio control is a basic control strategy which adjusts the duty ratio of switching devices on the primary-side of the converter by assigning a phase angle to each cell. The relationship between the voltage gain and duty ratio is illustrated in (5).

B. Phase shift control

The phase shift control is another control strategy used to regulate the output voltage. Because the proposed topology uses the series connection on the primary-side and the parallel connection on the secondary-side, there are two kinds of methods to realize the phase shift control.

(1) Phase shift control within a cell

As shown in Fig. 10, each cell is composed of two bridge arms and the phase angle between the two arms (φ_1) can be employed to regulate the output voltage. In Fig.10 (a), T_s stands for switching period of switching devices. There are controllable and uncontrollable areas for each cell. In the controllable area, the pulse width of V_{ab} is

related with the phase shift angle. In the uncontrollable area, the pulse width of V_{ab} is fixed at its maximum and is independent of the phase shift angle. The pulse voltage is $NV_{in}/(1\text{-}D)$ and the output voltage is maintained at its maximum. Therefore, the output voltage is stable regardless of changes in the phase shift angle. Fig. 10 (b) presents the simulation results for the phase shift control within cells. The input voltage is 15 V; load resistance is 20 Ω; switching frequency is 20 kHz, and duty ratio is 0.5. In Fig. 11, the phase shift angles are 120°. The phase shift angle for cells 1 and 2 is 180° and they have the same duty ratio for all switching devices. By controlling the bridge arm phase shift angle, the output voltage is regulated at will. The 120° phase shift and 240° phase shift have the same output voltage, verifying the correctness of Eqs. (6)-(7). The corresponding derive progress is illustrated in the appendix.

For the phase shift control in the controllable area, the secondary-side of the coupled inductor is equivalent to several Buck converters connected in series working at discontinuous conduction mode (DCM). The corresponding duty ratio of the Buck converter is $\varphi_1/2\pi$. Given the voltage gain of the Buck converter working in DCM, the output voltage is represented by:

$$V_{out} \approx \frac{2\cdot m\cdot \varphi_1}{2\pi}\cdot\frac{N\cdot V_{in}}{1-D} \quad (\varphi_1<\pi) \tag{6}$$

$$V_{out} = \frac{2\cdot m\cdot (1-\varphi_1)}{2\pi}\cdot\frac{N\cdot V_{in}}{1-D} \quad (\varphi_1\geq\pi) \tag{7}$$

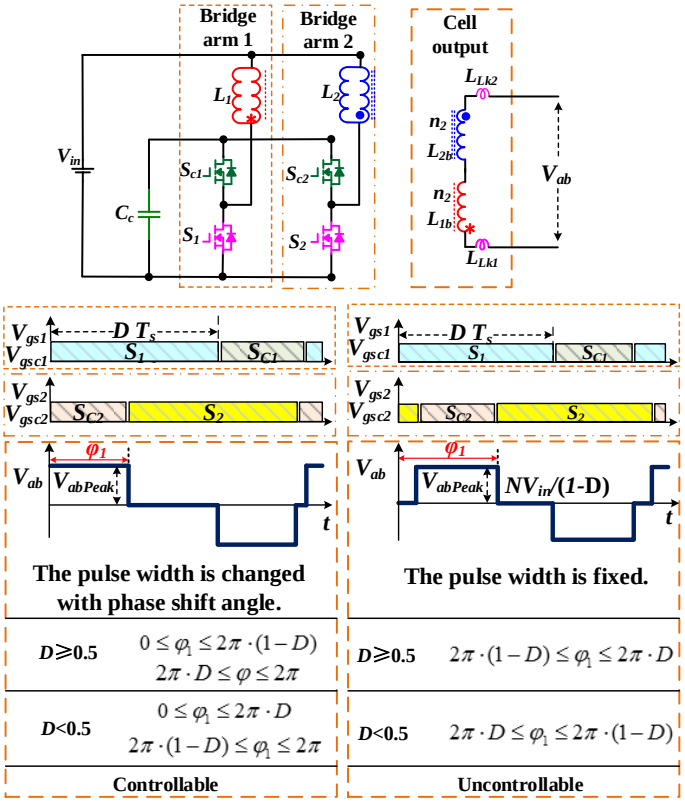

(a)

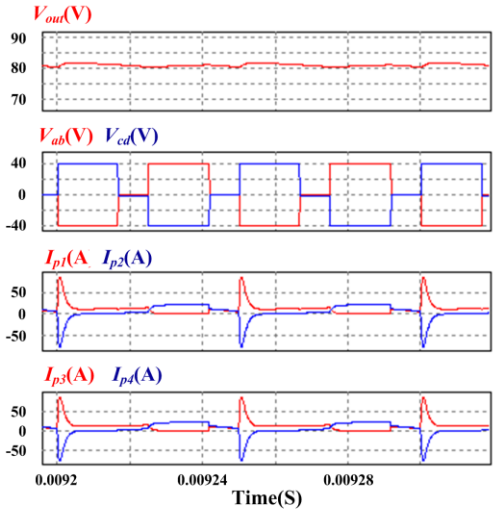

(b)

Fig. 10. Phase shift control within a cell. (a)Phase shift angle control analysis and (b) Simulation results of phase shift angle control within a cell (120° phase shift angle).

(2) Phase shift control between cells

In each cell, the corresponding terminal voltage is with the alternative voltage character. The series connection of cells form high alternative voltage and then rectified by the diodes. The phase angle among the cells can directly influence the converter output voltage. The phase shift control can also be employed to regulate the phase angle between cells. Fig.11 illustrates the energy transfer area and non-energy transfer area in phase shift control between cells. In Fig.11, φ_1 is the phase shift angle between bridge arms in the cell and φ_2 is the phase shift angle between cell-1 and cell-2. φ_1 is fixed. All cells in the bridge arms share the same duty ratio and the same phase shift angle, as shown in Fig. 11, in which each cell output is with same voltage waveform. By controlling φ_2, the energy transferred to the load can be regulated. In energy transfer area, the cell-1 and cell-2 voltage drop are in the reverse direction, in which both cell-1 and cell-2 supply energy to the load. In non-energy transfer area, the cell-1 and cell-2 voltage drop in the same direction, and the corresponding terminal voltage of converter is zero; therefore, no energy can be transferred to the load.

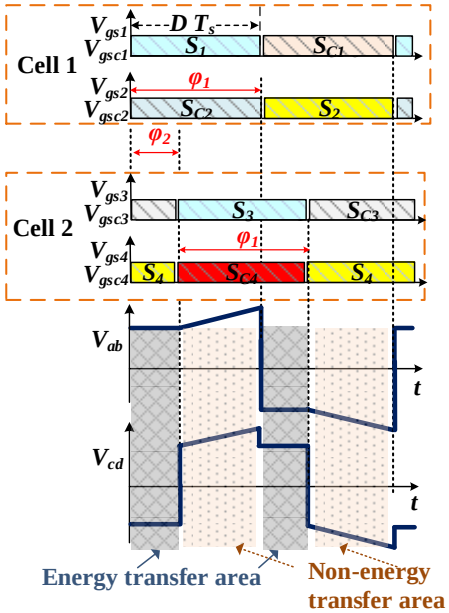

Fig. 11. The phase shift control strategy (between cells).

C. Redundancy operation

Under low voltage output or light load operating conditions, the main switches of each cell work with a low duty ratio and the converter efficiency is low. Furthermore, the converters need to be robust and reliable when working in harsh environments, such as offshore wind power transmission. The use of redundancy can increase the system reliability. There are two methods to achieve the redundancy operation.

(1) Cell idle operation

The first redundancy operation is to make one or more cells idle, for instance, reducing the cell number of a converter from *m* to *m-1*. As shown in Fig. 12 (a), a three-cell converter can be reduced to a two-cell converter by making cell 3 idle. The corresponding current flow state is illustrated in Fig. 12 (b) and Fig. 12 (c).

For the HVDC application, the voltage level is high; the number of the corresponding working cells is also large. When the number of working cells is large, the duty ratio or phase shift angle cannot be employed as the only control variable. The proposed topology has modular structure, and the modular cells can be switched on or switched off conveniently. Therefore, the number of working cells can also be employed to control the voltage output to achieve precise voltage control.

(2) Secondary-side hybrid parallel-series operation

The other redundancy operation is realized by a hybrid parallel-series connection. As shown in Fig. 13, cell-1 and cell-2 have the same phase angle; cell-3 has a 180° phase shift with respect to cell-1 and cell-2. In this mode, cell-1 and cell-2 are connected in parallel, and they are in series connection with cell-3. The power output of cell-3 is equal to the sum of the power output of cell-1 and cell-2.

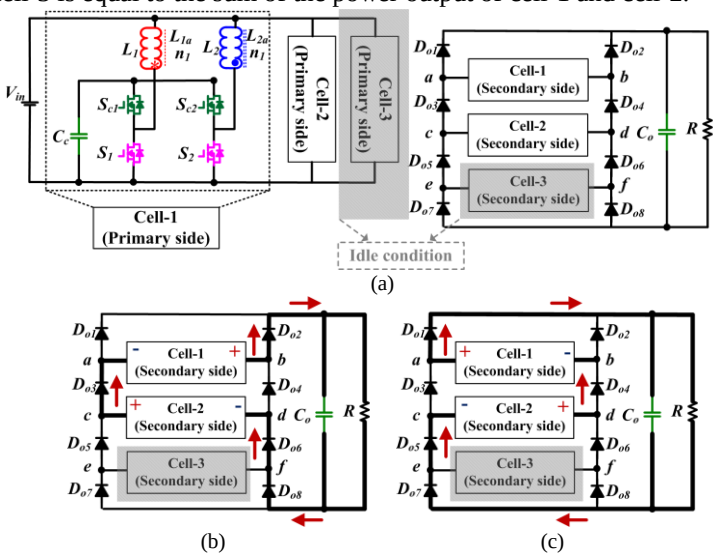

Fig. 12. Proposed cell idle operation strategy. (a) Idle condition for decreased output power/voltage. (b) Current flow state 1 and (c) Current flow state 2

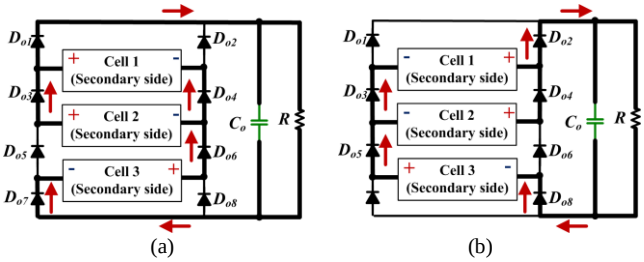

Fig. 13. Hybrid parallel-series operation. (a) Current flow state 1 and (b) Current flow state 2

D. Fault ride-through operation

The primary-side of the proposed topology is composed of switching devices, clamp capacitor, and coupled inductors. The secondary-side is composed of passive devices which are highly reliable. Because all the energy transferred to the secondary-side passes through the main switching devices, the main switching devices on the primary-side are prone to faults, especially under harsh operating conditions.

When S_1 is made open circuit as presented in Fig. 14(a), the system is operating in fault tolerance mode. In this case, main switching device S_2 turns off, and active clamp switching devices are turned on. There are two working states for the faulty cell, as presented in Fig. 14 (b) and Fig. 14 (c). Fig. 14(d) presents the simulations results. In the fault-ride-through operation, the faulty cell can still support output voltage.

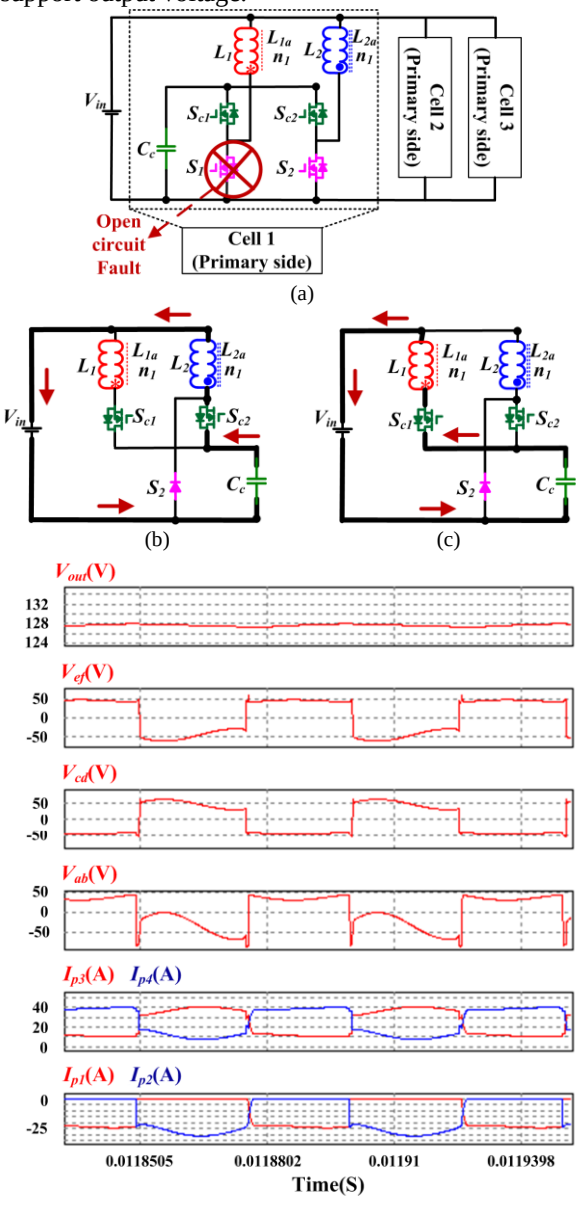

Fig. 14. Fault-ride-through operation. (a) Open circuit fault on the primary. (b) Faulty cell working state 1. (c) Faulty cell working state 2 and (d) Simulation results.

E. Current-sharing in the cases where inductors have non-uniform parameters

In the cell, due to the series connection of the two coupled inductors on the secondary-side, the current sharing can be achieved

naturally. Table I presents the current sharing characteristics in the cases where coupled inductors have non-uniform parameters. Even though there exist from parameter mismatches, the error of current sharing is limited to a low level.

TABLE I
ANALYSIS OF ASYMMETRICAL COUPLED INDUCTORS (TWO CELLS)

Inductance	Parameter	Case 1	Case 2	Case 3
Asymmetrical magnetizing inductance (L_{LK} =4 μH, N_p:N_s=1:2, f=20 kHz, 20 Ω load, Vin=15 V)	L_1 (μH)	35	35	35
	L_2 (μH)	35	35	35
	L_3 (μH)	35	30	35
	L_4 (μH)	25	30	45
	I_1 (A)	14.4	14.4	14.4
	I_2 (A)	14.4	14.4	14.4
	I_3 (A)	14.4	14.8	14.4
	I_4 (A)	15.3	14.8	14.1
	Current error $(I_1-I_4)/I_1$	-6.25%	-2.7%	2.08%
	Output voltage	87.9V	87.9V	87.8V

F. Influence of leakage inductance

The soft-switching of power devices can reduce the switching power losses and thus improve the energy efficiency of the converter. In order to realize zero voltage switching for the clamp switches, the antiparallel diodes of clamp switches should conduct before the switches are turned on. For the main switches, the energy stored in parasitic capacitors should be lower than that stored in the leakage inductor. The zero voltage switching turn-on condition for the main switches is

$$\frac{1}{2}\frac{L_{LKi}}{N_i^2}I_i^2 \geq \frac{1}{2}C_{DSi}V_{DSi}^2 \tag{8}$$

where I_i is the primary input current of the power step-up cell and C_{DSi} is the parasitic capacitor voltage. L_{LKi} is the sum of the leakage inductances.

G. Performance comparison

In order to demonstrate the advantages of the proposed topology, a performance comparison is carried out between the modular DC/DC topology, MMC DC/DC, and the proposed topology for offshore wind applications [15][24][34], which is summarized in Table II. It can be observed from the table that the proposed converter offers improvements on electrical isolation and superior fault tolerance capability compared with the modular DC/DC topology [15][24]. Moreover, the proposed converter shows improvements on power density and soft switching capability compared with the MMC DC/DC. The proposed converter needs more magnetic components than the other topologies, while thanks to the decentralized structure, the coupled inductor of the proposed converter have limited voltage stress and power level, which reduces the difficulty in manufacturing.

TABLE II
PERFORMANCE COMPARISON OF DIFFERENT CONVERTER TOPOLOGIES

Parameter	Converter in [24]	Converter in [15]	Converter in [34]	Proposed Converter
Modular topology	Yes	Partial modular	Yes	Yes
Structure scalability	No	No	Yes	Yes
Electrical isolation	No	No	Yes	Yes
Active switch voltage stress	2 V_{in}	V_{in}	V_{out}/N	$V_{in}/(1-D)$
Key energy transfer component	Capacitor inductance	Capacitor inductance	Capacitor and high-frequency transformer	Coupled inductor
Soft switching	Yes	Yes	No	Yes
Fault tolerance	No	No	Yes	Yes
Power density	High	High	Low	High

IV. EXPERIMENTAL VALIDATION

A 750-W DC/DC converter with three cells is developed to verify the proposed topology and corresponding control strategy, as shown in Fig. 15. For this system, the input voltage is set as 10~15 V, the output voltage is 100 V, the main switching devices and active clamping switching devices are FDP047AN and the corresponding switching frequency is 20 kHz. The secondary-side diodes are STTH6012W, the clamp capacitor is 10 μF, and the output capacitor is 470 μF. The coupled inductor parameters are shown in Table III. Arcol HS200 series aluminium housed axial panel mount resistors (100Ω ±1%), are employed to build load bank.

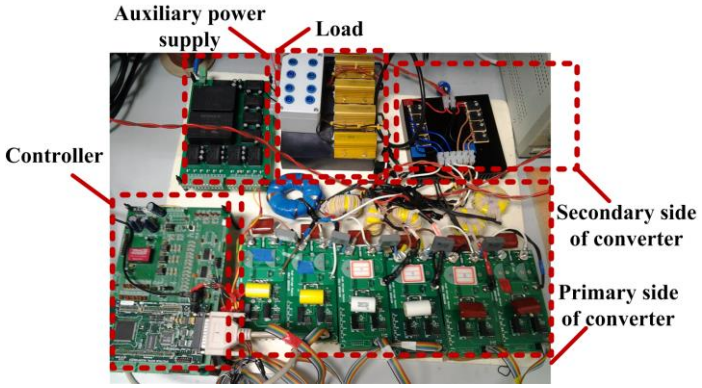

Fig. 15 Experimental platform

Fig. 16 presents the experimental results for the phase shift control within one cell of the two-cell converter. The driving signal is given in Fig. 16 (a). There is a 90° phase shift between the cells. Fig. 16 (b) shows the corresponding secondary currents. The experimental waveform of secondary current has the similar shape with the simulation results as shown in Fig. 10 (b). Fig. 17 presents the experimental results of the three-cell converter with non-uniform parameters for its coupled inductors. Because the coupled inductor L_6 has larger deviation in its excitation inductance and leakage inductance than L_1~L_5, the primary current of L_6 also has higher peak current than other coupled inductors, as shown in Fig. 17 (a). Fig. 17 (b) shows the corresponding secondary currents of the three cells. Owing to the series connection, the three cells share the same current naturally.

TABLE III
SPECIFICATIONS OF THE COUPLED INDUCTORS

		Primary excitation (μH)	Primary leakage (μH)	Secondary (μH)	Secondary leakage (μH)	Winding ratio Ns:Np
Cell-1	L_1	28.65	0.478	442.9	7.651	4:1
	L_2	29.27	0.480	453.5	7.684	4:1
Cell-2	L_3	28.88	0.480	447.3	7.684	4:1
	L_4	28.81	0.493	446.5	7.886	4:1
Cell-3	L_5	22.82	0.22	422.4	3.525	4:1
	L_6	29.12	0.483	456.5	7.912	4:1

Fig. 18 presents the results for fault tolerance operation. In Fig. 18 (a), the main switching devices of cell-3 are cut off to simulate an open-circuit fault, and the active clamp switching devices are still

operational. Fig. 18 (b) shows the secondary-side voltage output. Clearly, even though the main switching devices are faulted, the converter can still operate. Due to the parasitic capacitance, stray inductance and the ringing phenomenon, a 10V voltage peak can be observed in the voltage output of the cell. However, this phenomenon does not occur in the simulation results, because the parasitic capacitance in solid state devices and stray inductance in connecting wire have not been considered in the simulation condition. The waveform of experimental results matches with the simulations results shown in Fig.14 (d). Due to the parasitic capacitance, the ring phenomena are occurred that touch off a 10V voltage peak in the cell output voltage; while this phenomena isn't presented in the simulation, because the parasitic capacitance isn't considered in the simulation.

By controlling the phase shift angle of the primary-side devices, the proposed three-cell topology can sustain the secondary voltage output in parallel operation. There is no shift angle among three cells, and the converter is equivalent to the parallel operation of both primary-side and second-side. The corresponding output results are presented in Fig. 19 (a). Fig. 19 (b) shows the experimental results for the operation where cells 2 and 3 are connected in parallel and then in series with cell 1. As shown in Fig. 19 (b), the peak current of cell 1, cell 2 and cell 3 is 25 A, 10 A and 15 A, respectively. The difference between cells 2 and cell 3 is caused by the parameter difference in their coupled inductors, as shown in Table III. Due to the series connection of cell 1 and cells 2-3, the primary current of cell-1 is the sum of the primary current of cell 2 and cell 3.

Fig. 20 presents the working condition of the switching devices. Fig. 20 (a) shows the voltage stress on the secondary-side diodes; the terminal rectification diodes voltage stress is only half of the middle rectification diodes. The voltage stress on the middle rectification diodes is the sum of the output voltage from two cells. Fig. 20 (b) shows the switching characteristics of the main switching devices. Because of the active clamp structure, the voltage stress is limited and zero voltage switching is achieved. Compared with simulation waveforms, fluctuation is found in the waveforms of switching devices during switching on condition, which is caused by the resonance of leakage inductance and parameter capacitance.

Fig. 21 presents the efficiency of the proposed converter. When the power output is low (<500 W), the two-cell converter has higher efficiency than the three-cell converter. The three-cell converter has higher efficiency than the two-cell converter when the power output is high (>500 W). Owing to the flexible control of the proposed converter, the converter is capable of tracking the fluctuating wind power input for offshore wind power transmission. It should be pointed out that the operating voltage range of the prototype converter is 10-100 V, which is significantly lower than the level of practical wind farm systems. The adverse effect of diode bridges on the efficiency can be dramatically reduced if the converter is designed for the DC/DC conversion from LV to MV.

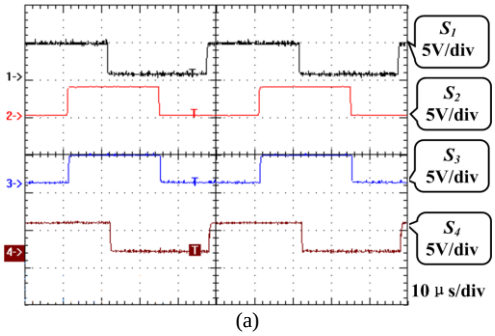

(a)

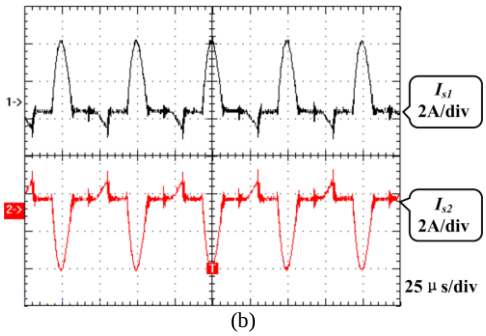

(b)

Fig. 16. Experiment results for the phase shift control. (a) Drive signal and (b) Secondary current.

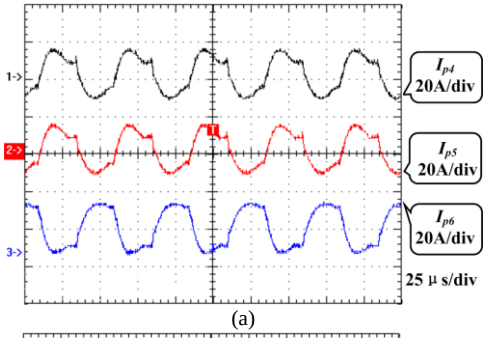

(a)

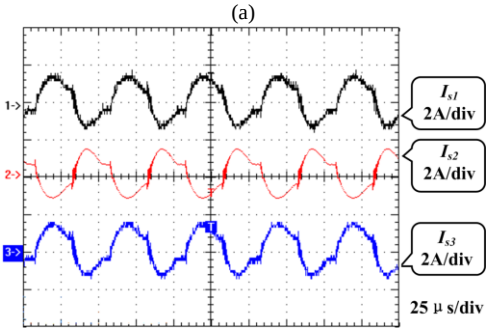

(b)

Fig. 17. Influence of non-uniform coupled inductance parameters. (a) Primary currents and (b) Secondary currents.

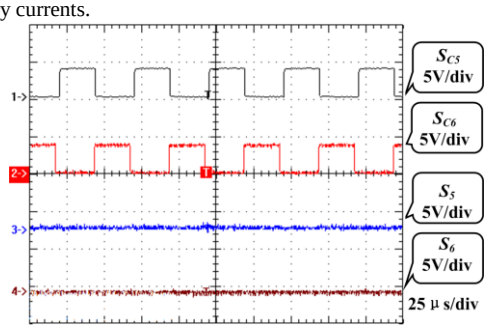

(a)

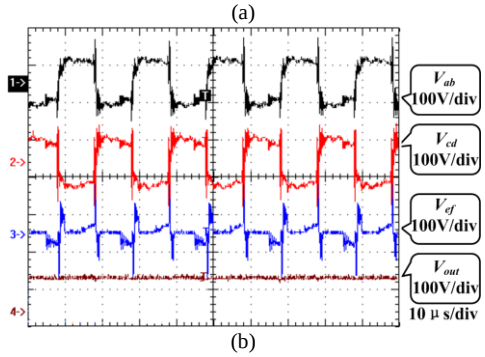

(b)

Fig. 18. Fault tolerant operation. (a) Fault cell drive signal and (b) Secondary output voltage.

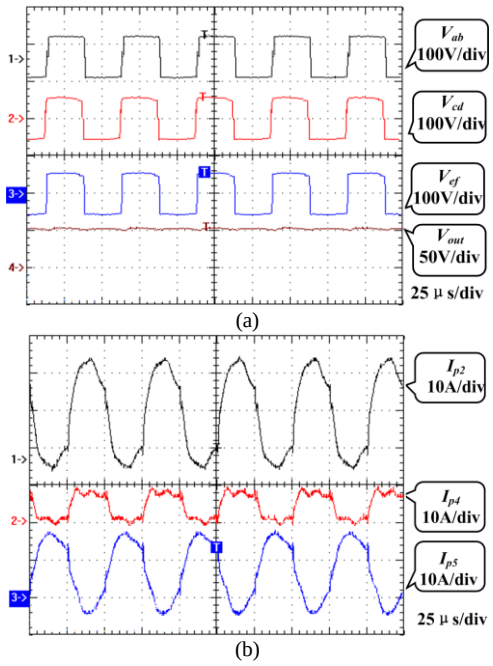

Fig. 19. Operation under a flexible parallel-series connection. (a) Three-cell parallel operation and (b)Two-cell parallel and 1 cell series connection

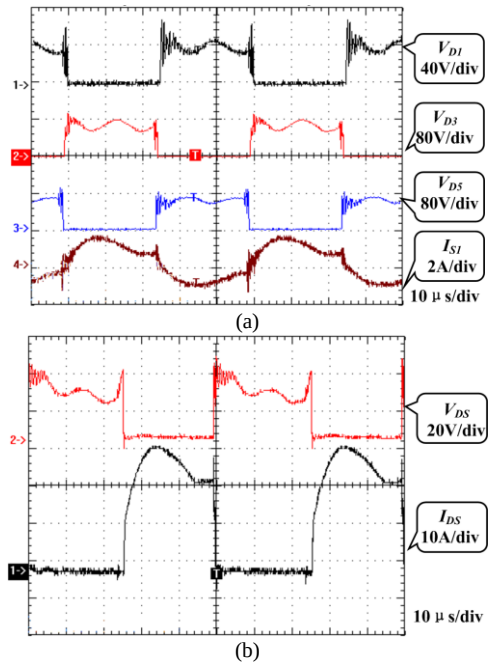

Fig. 20. Operation conditions of the switching devices. (a) Voltage stress on the secondary side diodes and (b) Soft switching.

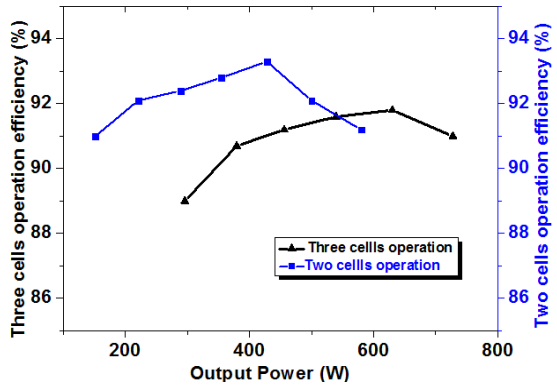

Fig. 21. Converter efficiency.

V. Conclusions

This paper has presented a modular DC/DC converter with an ultra-high voltage step-up ratio, which can be utilized for the interconnection of offshore wind farms with the HVDC transmission networks. The converter utilizes the flyback-forward topology in the basic converter cells, and then a high voltage conversion ratio is built up with the basic converter cells. From the results of theoretical analysis, simulation, and experimental tests, the proposed converter is effective and reasonably efficient. The key features of the proposed converter are summarized as follows,

(1) It has a modular and scalable structure with little stress on power devices on both the primary-side and the secondary-side.

(2) In order to capture the fluctuating wind energy, the proposed topology incorporates PWM control, phase shift control, and redundancy operation to improve the efficiency and control flexibility of the DC/DC conversion system.

(3) The proposed converter has fault tolerance operating capability, which suits harsh operating conditions of the offshore wind power transmission system.

References

[1] H. Ergun, D. Van Hertem, and R. Belmans, "Transmission system topology optimization for large-scale offshore wind integration," *IEEE Trans. Sustain. Energy*, vol. 3, no.4,pp. 908-917,Oct. 2012.

[2] L. Hanchao and S. Jian, "Voltage stability and control of offshore wind farms with AC collection and HVDC transmission," *IEEE Journal of Emerging and Selected Topics in Power Electronics*, vol. 2, no.4,pp. 1181-1189, Dec. 2014.

[3] R. E. Torres-Olguin, M. Molinas, and T. Undeland, "Offshore wind farm grid integration by VSC technology with LCC-based HVDC transmission," *IEEE Trans. Sustain. Energy*, vol. 3, no.4,pp. 899-907, Oct. 2012.

[4] R. E. Torres-Olguin, A. Garces, M. Molinas, and T. Undeland, "Integration of offshore wind farm using a Hybrid HVDC transmission composed by the PWM current-source converter and line-commutated converter," *IEEE Trans. Energy Convers.*, vol. 28, no.1, pp. 125-134, Mar. 2013.

[5] N. Flourentzou, V. G. Agelidis, and G. D. Demetriades, "VSC-based HVDC power transmission systems: an overview," *IEEE Trans. Ind. Appl.*, vol. 24, no.3, pp. 592-602, Mar. 2009.

[6] L. Xu, L. Yao, and C. Sasse, "Grid integration of large DFIG-based wind farms using VSC transmission," *IEEE Trans. Power Sys.*, vol. 22, no.3, pp. 976-984, Aug. 2007.

[7] G. J. Kish, M. Ranjram, and P. W. Lehn, "A modular multilevel DC-DC converter with fault blocking capability for HVDC interconnects," *IEEE Trans. Power Electron.*, vol. 30, no.1,pp. 148-162, Jan. 2015.

[8] S. M. Muyeen, R. Takahashi, and J. Tamura, "Operation and control of HVDC-connected offshore wind farm," *IEEE Trans. Sustain. Energy*, vol. 1, no.1, pp. 30-37, Apr. 2010.

[9] A. Egea-Alvarez, F. Bianchi, A. Junyent-Ferre, G. Gross, and O. Gomis-Bellmunt, "Voltage control of multiterminal VSC-HVDC transmission systems for offshore wind power plants: design and implementation in a scaled platform," *IEEE Trans. Ind. Electron.*, vol. 60, no.6, pp. 2381-2391, Jun. 2013.

[10] P. Bresesti, W. L. Kling, R. L. Hendriks, and R. Vailati, "HVDC connection of offshore wind farms to the transmission system," *IEEE Trans. Energy Convers.*, vol. 22, no.1, pp. 37-43, Mar. 2007.

[11] J. Liang, T. Jing, O. Gomis-Bellmunt, J. Ekanayake, and N. Jenkins, "Operation and control of multiterminal HVDC transmission for offshore wind farms," *IEEE Trans. Power Del.*, vol. 26, no.4, pp. 2596-2604, Oct. 2011.

[12] M. Liserre, R. Cardenas, M. Molinas, and J. Rodriguez, "Overview of multi-MW wind turbines and wind parks," *IEEE Trans. Ind. Electron.*, vol. 58, no.4, pp. 1081-1095, Apr. 2011.

[13] Y. Gu, X. Xin, W. Li, X. He, "Mode-adaptive decentralized control for renewable DC microgrid with enhanced reliability and flexibility," *IEEE Trans. Power Electron.*, vol. 29, no. 9, pp. 5072-5080, Sep. 2014.

[14] Y. Jin, J. E. Fletcher, and J. O'Reilly, "Multiterminal DC wind farm collection grid internal fault analysis and protection design," *IEEE Trans. Power Del.*, vol. 25, no.4, pp. 2308-2318, Oct. 2010.

[15] W. Chen, A. Q. Huang, C. Li, G. Wang, and W. Gu, "Analysis and comparison of medium voltage high power DC/DC converters for offshore wind energy systems," *IEEE Trans. Power Electron.*, vol. 28, no.4, pp. 2014-2023, Apr. 2013.

[16] C. Meyer, M. Hoing, A. Peterson, and R. W. De Doncker, "Control and design of DC grids for offshore wind farms," *IEEE Trans. Ind. Appl.*, vol. 43, no.6, pp. 1475-1482, Nov.-Dec. 2007.

[17] W. Li, Y. Zhao, Y. Deng, X. He, "Interleaved converter with voltage multiplier cell for high step-up and high efficiency conversion," *IEEE Trans. Power Electron.*, vol. 25, no.9, pp. 2397-2408, Sep. 2010.
[18] H. R. E. Larico and I. Barbi, "Three-phase weinberg isolated DC-DC converter: analysis, design, and experimentation," *IEEE Trans. Ind. Electron.*, vol. 59, no. 2, pp. 888-896, Feb. 2012.
[19] C. Liu, A. Johnson, J.S. Lai, "A novel three-phase high-power soft-switched DC-DC converter for low voltage fuel cell applications," *IEEE Trans. Ind. Appl.*, vol. 41, no.6, pp. 1691-1697, Nov/Dec. 2005.
[20] W. Li and X. He, "Review of nonisolated high-step-up DC/DC converters in photovoltaic grid-connected applications," *IEEE Trans. Ind. Electron.*, vol. 58, no. 4, pp. 1239-1250, Apr. 2011.
[21] I. A. Gowaid, G. P. Adam, A. M. Massoud, S. Ahmed, D. Holliday, and B. W. Williams, "Quasi two-level operation of modular multilevel converter for use in a high-power DC transformer with DC fault isolation capability, " *IEEE Trans. Power Electron.*, vol. 30, no. 1, pp. 108- 123, Jan. 2015.
[22] D. Montesinos-Miracle, M. Massot-Campos, J. Bergas-Jane, S. Galceran-Arellano, and A. Rufer, "Design and control of a modular multilevel DC/DC converter for regenerative applications." *IEEE Trans. Power Electron.*, vol. 28, no. 8, pp. 3970- 3979, Aug. 2013.
[23] V. Vlatkovic, J. A. Sabate, R. B. Ridley, F. C. Lee, and B. H. Cho, "Small-signal analysis of the phase-shifted PWM converter," *IEEE Trans. Power Electron.*, vol. 7, no.1, pp. 128- 135, Jan. 1992.
[24] A. Parastar and J. K. Seok, "High-gain resonant switched-capacitor cell-based DC/DC converter for offshore wind energy systems," *IEEE Trans. Power Electron.*, vol. 30, no. 2, pp. 644 - 656, Feb. 2015.
[25] J. Robinson, D. Jovcic, and G. Joos, "Analysis and design of an offshore wind farm using a MV DC grid," *IEEE Trans. Power Del.*, vol. 25, no. 4, pp. 2164-2173, Oct. 2010.
[26] N. Denniston, A. Massoud, S. Ahmed, and P. Enjeti, "Multiple-module high-gain high-voltage DC-DC transformers for offshore wind energy systems," *IEEE Trans. Ind. Electron.*, vol. 58, no. 5, pp. 1877-1886, May 2011.
[27] X. Zhang, T. C. Green, "The modular multilevel converter for high step-up ratio DC-DC conversion," *IEEE Trans. Ind. Electron.*, vol. 62, no. 8, Aug. 2015.
[28] S. V. Araújo, R. P. Torrico-Bascopé, and G. V. Torrico-Bascopé, "Highly efficient high step-up converter for fuel-cell power processing based on three-state commutation cell," *IEEE Trans. Ind. Electron.*, vol. 57, no. 6, pp. 1987-1997, Jun. 2010.
[29] G. C. Silveira, F. L. Tofoli, L. D. S. Bezerra, and R. P. Torrico-Bascopé, "A nonisolated DC–DC boost converter with high voltage gain and balanced output voltage," *IEEE Trans. Ind. Electron.*, vol. 61, no. 12, pp. 6739- 6746, Dec. 2014.
[30] S. P. Engel, M. Stieneker, N. Soltau, S. Rabiee, H. Stagge, and R. W. De Doncker, "Comparison of the modular multilevel DC converter and the dual-active bridge converter for power conversion in HVDC and MVDC grids," *IEEE Trans. Power Electron.*, vol. 30, no. 1, pp. 644 - 656, Feb. 2015.
[31] K. C. Tseng, J. Z. Chen, J. T. Lin, C. C. Huang, and T. H. Yen, "High step-up interleaved Forward-Flyback boost converter with three-winding coupled inductors," *IEEE Trans. Power Electron.*, vol. 30, no. 9, pp. 4696-4703, Sep. 2015.
[32] M. Hajian, J. Robinson, D. Jovcic, and B. Wu, "30 kW, 200 V/900 V, thyristor LCL DC/DC converter laboratory prototype design and testing," *IEEE Trans. Power Electron.*, vol. 29, no. 3, pp. 1094-1102, Mar. 2014.
[33] J. A. Ferreira, "The multilevel modular DC converter," *IEEE Trans. Power Electron.*, vol. 28, no. 10, pp. 4460-4465, Oct. 2013.
[34] T. Luth, M. M. C. Merlin, T. C. Green, F. Hassan, C. D. Barker, "High-frequency operation of a DC/AC/DC system for HVDC applications," *IEEE Trans. Power Electron.*, vol. 29, no. 8, pp. 4107-4115, Aug. 2014.
[35] X. K. Wu, C. Hu, J. Zhang, C. Zhao, "Series–parallel autoregulated charge-balancing rectifier for multioutput Light-Emitting Diode Driver," *IEEE Trans. Ind. Electron.*, Vol. 61, no.3, pp. 1262-1268, Mar. 2014.
[36] B. R. Lin, J. Y. Dong, and J.-J. Chen, "Analysis and Implementation of a ZVS/ZCS DC–DC switching converter With Voltage Step-Up," *IEEE Trans. Ind. Electron.*, vol.58, no.7, pp. 2962-2971, Jul. 2011.
[37] Y. Hu, R. Zeng, W. Cao, J. Zhang, S. Finney, "Design of a High-power, High Step-up Ratio Modular DC-DC Converter by the Matrix Transformer Approach," *IEEE Trans. Ind. Electron.*, vol. pp, no.99, 2016.
[38] J. Wang, T. Zhao, J. Li, A.Q. Huang, R.Callanan, F. Husna, A. Agarwal, "Characterization, modeling, and application of 10-kV SiC MOSFET," *IEEE Trans. Electron Devices*, vol. 55, no. 8, pp.1798-1806, Jul. 2008.

VI. Appendix

From the waveform of the leakage inductor current, the secondary side of the coupled inductor is equivalent to a discontinuous conduction mode (DCM) of a Buck converter.

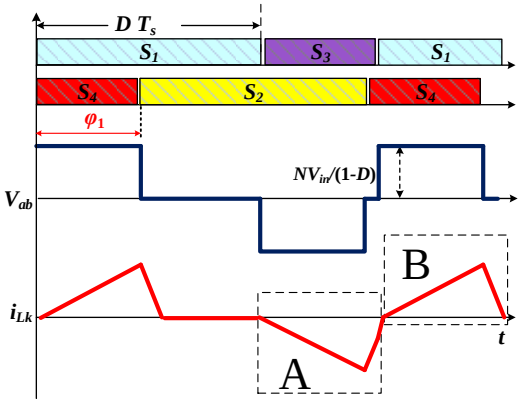

Fig. A1 Cell operation analysis

For pulse A, the current decreases to the negative peak value and increases to zero at the time of $(1\text{-}D)T_s$. The decrement time is equal to $T_s\varphi_1/2\pi$ and the increment time is $(1-D-\varphi_1/2\pi)T_s$. Following the voltage-second balance (Eq.A1), the critical phase angle can be determined by Eq. A2. The secondary side of the coupled inductor is equivalent to two Buck converters connected in parallel at the DCM operational condition. The corresponding equivalent duty ratio of the Buck converter is $\varphi_1/2\pi$. Provided the voltage gain of the Buck converter in DCM, the output voltage is given as Eq. A3.

$$\frac{N\cdot V_{in}}{1-D}\cdot\frac{\varphi_1}{2\pi}\cdot T_s = V_{out}(D-\frac{\varphi_1}{2\pi})T_s \tag{A1}$$

$$\varphi_1 = \pi\cdot D\cdot(1-D)\cdot\frac{V_{out}}{N\cdot V_{in}} \tag{A2}$$

$$V_{out} = \frac{2}{1+\sqrt{1+\dfrac{4\cdot 2L_k}{R_o\cdot T_s\cdot(\varphi_1/2\pi)^2/2}}}\cdot\frac{N\cdot V_{in}}{1-D} \approx \frac{2\cdot m\cdot\varphi_1}{2\pi}\cdot\frac{N\cdot V_{in}}{1-D} \tag{A3}$$